Development and Validation of Whole-Body Finite Element Occupant and Pedestrian Models of a 70-Year-Old Female

Xin Jin, Anil Kalra, Anand Hammad, Prashant Khandelwal, Vaibhav Porwal, Ming Shen, King H. Yang

Abstract Elderly females are vulnerable to severe injury and mortality during vehicle collisions. The current increase in the population of elderly people means there is an urgent need to address the safety-related issues relevant to elderly occupants. However, current anthropomorphic surrogates, like dummies, cannot be directly used to study injury prevention for elderly females because they lack the necessary age- and gender-based impact responses.

This study aimed to develop two finite element models of a 70-year-old female (named CHARM-70F) in a driving and a standing posture. The finite element mesh of CHARM-70F was developed through computer tomography (CT) scans of an elderly female cadaver. The data included for validation of the CHARM-70F model was taken from the published experimental studies for elderly female specimens. The component level validations were conducted on the major body regions, including head, neck, thorax, abdomen, pelvis, and extremities. Then the standing and driving posture models were validated at the whole-body level. In both component and whole-body level impact scenarios, reasonable agreements were obtained. The CHARM-70F models are validated numerical surrogates and will be further used to study the gender- and age-related injury mechanisms and prevention for this vulnerable population.

Keywords Finite element method, Whole-body human model, CHARM-70F, Elderly female, Model validation.

I. INTRODUCTION

As a vulnerable population, elderly females require special attention in terms of their traffic-related safety. According to the National Highway Traffic Safety Administration (NHTSA), the fatality risk of a 75-year-old (yo) female occupant is 3.87–5.67 times higher than that of a 21yo occupant [1]. This study also showed that although elderly female drivers (aged 65–74 years) are at similar levels of risk as elderly male drivers of the same age group, the fatality risk for elderly female passengers is 11.4% higher than for elderly male passengers.

In a UK study in which statistical analyses were conducted for accidents involving injuries, Lenard and Welsh [2] reported that front-row female occupants were more vulnerable than male drivers, especially with regard to skeletal chest injuries, during frontal crashes. Roberts and Compton [3] established the relationship between delta-V (the change in car speed) and injuries for more than 20,000 accidents. It was found that the median level of AIS (Abbreviated Injury Scale) 3+ injuries occurred at 38 km/h in females and at 44 km/h in males. Bose *et al*. [4] conducted a multivariate regression analysis with different factors, such as age, mass, BMI category, delta-V, etc. They found that in comparable crash conditions, the injury risk to female drivers was 38% and 67% higher than that to male drivers for chest and spine injuries, respectively.

Wang *et al*. [5] studied the risk of AIS3+ injuries using the Crash Injury Research and Engineering Network (CIREN) for elderly occupants aged 60 and older. The results revealed that the thorax, lower extremities and upper extremities were at greater risk in the elderly population, as shown in Fig. 1.

From all the studies mentioned above, it is clear that injury risks to elderly females are different from those posed to younger adults or even elderly males in vehicle crashes. The reason for this difference can result from both age and gender, which play significant roles in changing injury tolerances in various body regions. For example, the rib angle (from the superior-most posterior point of the rib, to the superior-most anterior point of the rib) changes with age and gender [6-8]. Kalra *et al.* [9] reported the compositional change in rib cortical bone thickness as a function of both age and gender. A recent study by Holcombe et al. [10] performed multivariable regression analysis to characterize the independent effect of age, sex, height, and weight on the

X. Jin (e-mail: xin.jin@wayne.edu; tel: +1 313 577 0422) is a Research Assistant Professor, A. Kalra and M. Shen are Graduate Research Assistants and A. Hammad, P. Khandelwal and V. Porwal are Student Assistants in Biomedical Engineering, all at Wayne State University, USA. K. H. Yang is a Professor and Director of the Bioengineering Center at Wayne State University.

rib shape and orientation. A statistical rib shape and orientation model was also developed from that study. Moreover, the interaction effects of age and gender in the change of Young's modulus of cortical and cancellous bones, as a result of bone mineral density loss, has been reported in several studies [11-12]. There is an urgent need to develop different strategies to study injury thresholds and prevention for this vulnerable population.

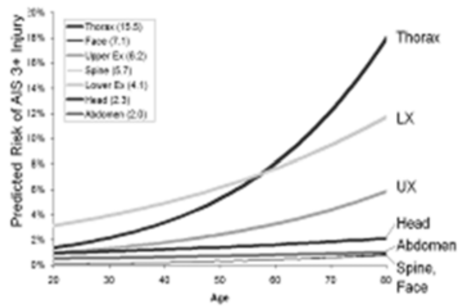

Fig. 1. Predicted risk of AIS3+ injury by different body regions versus age groups in frontal crashes for belted drivers at 30 mph crash speed (from Wang *et al*. [5]).

The only available study of elderly female finite element (FE) modeling was published by Iwamoto *et al.* [13]. It was modified from the 5th percentile THUMS model for the adult female (THUMS AF05) with active muscle responses. Material properties of skeletal parts with low strength were input into the model, to represent elderly people. The thorax and abdomen of this elderly AF05 model were validated against cadaver test data obtained from frontal impacts. The head and neck responses were validated during a low-speed, rear-end impact. There has been no further validation work or application of the model reported.

Antona-Makoshi *et al*. [14] developed a full-body FE model for Japanese elderly males. Age-dependent properties were assigned to the rib cage and the thoracic flesh materials. The model was validated against thorax impacts and frontal sled impacts. Material properties of the ribs, flesh, and costal cartilage were identified to affect rib cage deformation and risks of rib fractures.

Schoell et al. [15] developed a full-body FE model for an average elderly male (M50 65YO). This model was morphed from the average male model of Global Human Body Model Consortium (GHBMC M50). Age-dependent material properties and cortical thickness were assigned. Impact validation tests were performed in several regions including, chest, shoulder, thoracoabdominal, and pelvis. In a frontal US NCAP simulation, this elderly model predicted higher injury risks for the head and thorax compared to M50.

As a result, FE models for elderly females that represent age- and gender-dependent changes in impact response are necessary. There are two objectives in the current study. The first objective is to develop whole-body FE occupant and pedestrian models representative of a 70yo average elderly female. The model was named CHARM-70F (the Collaborative Human Advanced Research Models). The second objective is the segmental and whole-body level model validation, in order to evaluate the biofidelity of the models.

II. METHODS

Model Development

An average 70yo female has anthropometric measurements of 1.60 m in height and 73 kg in weight, based on statistical results from Centers for Disease Control and Prevention (CDC) [16]. A female cadaver of 73yo with a height of 1.58 m and weight of 62 kg was selected to extract skeleton geometry from CT scan images. In addition, contrast CT scanned data of a 65yo female patient were retrieved from an online database (www.cancerimagingarchive.net). These data were used to extract the geometry of the heart, lungs, liver, kidneys, pancreas, spleen, gall bladder, aorta, vena-cava, and the rest of the abdominal tissues. After collecting the medical images, the 3D rendering of the scanned slices was done using Mimics (Ver. 12.0, Materialise, Leuven, Belgium) and the computer-aided design (CAD) surfaces of the skeleton and internal organs were retrieved.

Finally, external body surfaces of driving and standing postures were obtained from a database that was developed from an anthropometric study reported by Reed *et al*. [17] at the University of Michigan Transportation Research Institute (UMTRI). The skeletal meshes were integrated with the outer body surface using the landmarks at the joint locations and key identifiable points at different body regions, such as the scapula, elbow, shoulder, pubic symphysis, etc.

To ensure that the skeletal geometric characteristics obtained from the CT scan were a true representation of the population average, adjustments were made based on a study by Shi *et al*. [18]. In the study, a statistical model accounting for variations such as age, gender, height and BMI was developed to define the average geometry of the human rib cage. The original post mortem human subject (PMHS) rib-cage geometry was found to be approximately 5% smaller in depth and 10% smaller in width (Fig. 2). The final rib-cage geometry was adjusted to match the statistical model. Finally, internal organs were scaled, along with the ribcage and abdominal cavity.

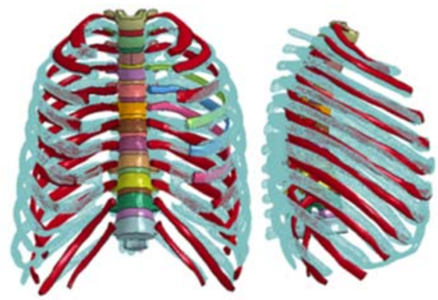

Fig. 2. Comparison between the PMHS geometry (red) and the statistical model developed by Shi *et al*. (cyan).

Compositional characteristics of cortical bone thickness play a critical role in impact responses. The cortical thicknesses of the major bony structures, such as the skull and long bones, were obtained directly from CT scans. However, the cortical thickness of ribs in elderly females is on average less than 1 mm, and cannot be easily determined from CT scans taken with commonly used resolutions. In addition, the average thickness of the rib cortical bone has been reported to vary along the length of the structure [19-20]. Weaver *et al.* [21] conducted a morphometric analysis on variations in sizes and shapes of ribs with respect to age and gender, based on CT scans of 339 subjects. Kalra et al. [9] reported the age- and gender-related average rib cortical thickness from 278 rib samples taken from 82 cadavers. The rib cortical thickness at the anterolateral portion was reported as 0.94 mm. Further, the scaling factors along the length of the rib on 5 sub-regions were provided by Dr. Weaver through personal communication. The regional cortical thickness was then obtained, as shown in Table I. A gradually transitional nodal thickness at the junction of adjacent sections was assigned at 3-4 junction nodes so that the stress concentration due to sudden change in the cortical thickness can be avoided. The complete details of chest cortical thicknesses assignment and material model development are reported in [22].

TABLE I

SCALING FACTORS OF THICKNESS DISTRIBUTION AND DEFINED THICKNESSES IN CHARM-70F FOR ENTIRE RIB LENGTH

Location	Posterior	Posterolateral	Lateral	Anterolateral	Anterior
Scaling factor	100%	126.83%	134.15%	102.44%	74.39%
Defined cortical thickness (mm)	0.91	1.15	1.21	0.94	0.68

The hexahedral FE mesh of CHARM-70F was developed using ANSYS ICEM (ANSYS Inc. Canonsburg, PA), a pre-processor based on a multi-block meshing scheme aimed at hexahedral mesh generation. Most of the bony structure was modeled as hexahedral mesh for trabecular bone, while shell elements were used to represent cortical bone. Some cavities in the thoracic and abdominal regions were built using tetrahedral elements. The ligaments at different anatomical locations were modeled using 1D tension-only elements. The finalised mesh for skeletal bones fit into the outer body surface provided by UMTRI. The landmarks for the joint locations and key identifiable points at different regions of the body, like scapula, elbow, shoulder, pubic symphysis, etc. were provided by the group for positioning the skeletal structures in the outer body surface. Based on these landmarks, appropriate meshed components of the skeletal bones (such as the sternum, thoracic spine, lumbar spine and other bones) were integrated with the outer surface.

Validation

Model validations were conducted at both component and whole-body levels to ensure biofidelity of the impact responses. It should be noted that all the experimental data chosen for CHARM-70F validation were from elderly female (>60yo) PMHS. Table II summarises the validation matrix, including the body regions, loading conditions, validation targets and the referenced studies.

Objective Evaluation and Injury Prediction

The ISO/TS 18571 standard was applied to quantitatively compare the time histories of simulation results to experimental data. The ISO standard yields a weighted score based on four metrics: corridor, phase, magnitude and slope. The ISO score ranges from 0 to 1, with 1 representing a perfect fit and 0 representing a poor fit.

Besides the ISO score, bone fractures in a selection of bony structures were also simulated and compared with experimental data. In the CHARM-70F model, element deletion method was used to simulate fractures by removing the elements on which the specific strain threshold was exceeded. These thresholds were obtained from the literature and adjusted in segmental validations to achieve similar fracture results.

TABLE II
SUMMARY OF COMPONENT AND WHOLE-BODY VALIDATIONS FOR CHARM-70F

Body region	Loading type	Part/FE Model Involved	Validation Target	Sample Size	Referenced Study
Head	Linear acceleration	Skull and Brain	Intracranial pressure at different regions	4	Nahum *et al.* (1977) [23]
	Facial impact on zygoma, maxilla, and frontal bone	Head	Impact force and peak force at fracture	zygoma:4 maxilla:5 frontal: 9	Allsop (1988) [24]
	Rotation	Head	Brain/skull relative motion	5	Hardy *et al.* (2007) [25]
Neck	Axial compression	Head and neck	Impact force	2	Nightingale *et al.* (1997) [26]
	Whiplash loading	Head and neck	Head rotation vs time	2	Deng *et al.* (2000) [27]
Thorax	Pendulum loading	Isolated ribcage	Force-deflection	3	Vezin and Berthet (2009) [28]
	Single Belt loading Hub loading Double belt loading	Upper torso	Force-deflection	6	Kent *et al.* (2004) [6]
	Pendulum loading	Whole body	Force-deflection	3	Kroell *et al.* (1971) [29]
Pelvis	Pendulum loading	Whole body	Force-deflection	2	Talantikite *et al.* (1998) [30]
	Lateral impact to acetabulum	Isolated Pelvis	Peak force and displacement	6	Guillemot *et al.* (1997) [31]
Abdomen	Rigid bar intrusive loading	Whole body	Force-deflection	2	Cavanaugh *et al.* (1986) [32]
	Lateral pendulum impact	Whole body	Peak force	2	Ramet and Cesari (1979) [33]
Lumbar	Flexion and Extension	Isolated lumbar	Bending moment vs angle	1	Demetropoulos *et al.* (1999) [34]
Lower extremity long bones	Femur three-point bending	Femur bone	Force-deflection and peak force at fracture	1-3	Kerrigan *et al.* (2003) [35]
	Tibia impact	Lower extremities	Peak impact force	3	Viano *et al.* (1978) [36]
Knee	Knee bolster impact	Lower extremities	Peak impact force	3	Viano *et al.* (1978) [36]

	Knee-thigh-hip complex impact	Lower extremities	Time history of impact force	5	Rupp *et al.* (2002) [37]
Upper extremity long bones	Humerus three-point bending	Humerus and flesh	Peak moment	4	Duma *et al.* (1999) [38]
	Forearm three-point bending	Forearm	Time history of impact force and strain	7	Duma *et al.* (1999) [38]
Whole body	Frontal sled test	Whole body	Seat belt forces and number of rib fractures regardless of location	1	Petitjean *et al.* (2002) [39]
	Lateral sled test	Whole body	Impact forces at different regions	6	Wood *et al.* (2014) [40]

III. RESULTS

Figure 2 displays the mesh of the CHARM-70F models. The general information and mesh qualities of the model are listed in Table III.

Fig. 2. CHARM-70F occupant (right) and pedestrian (left) models.

TABLE III

CHARM-70F SUMMARY STATISTICS AND MESH QUALITIES

Number of parts	Number of nodes	Number of elements	Time step size
582	870,943	1,506,193	1.03e-4 ms
	Acceptance Criterion	CHARM-70F Fulfilled	
Time step	0.1e-6 s	0.103e-6 s	
Warpage	< 50	> 99 %	
Aspect Ratio	< 5	> 99 %	
Skew	< 60	> 99 %	
Jacobian	> 0.3	> 99 %	

Simulation Results

All component level validation results are shown in Appendix B. The model response sequences for all whole-body level impact validations are shown in Fig. 3. For each simulation, the model response of CHARM-70F is plotted against the experimental results of elderly female subjects (Fig. 4).

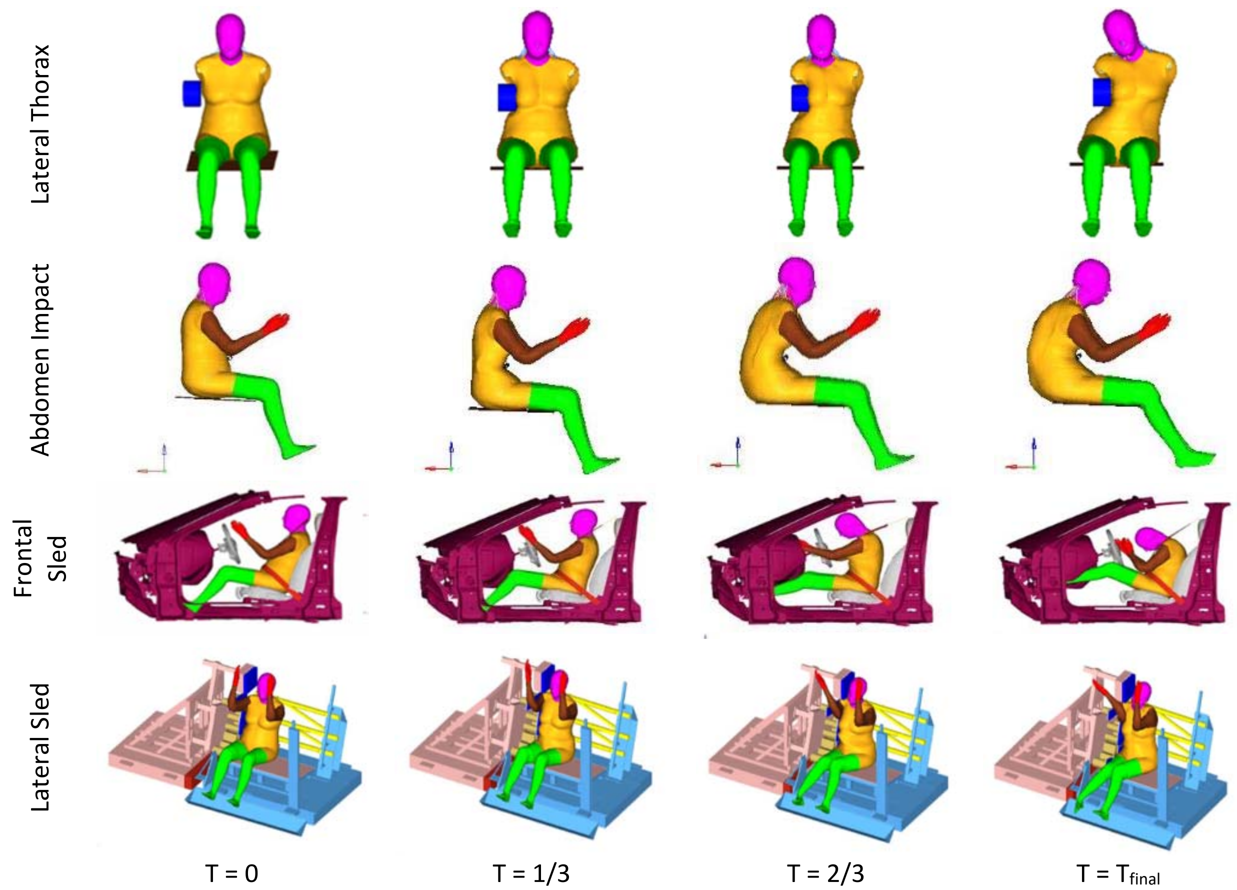

Fig. 3. Simulation time-lapse for whole-body level impact validation cases.

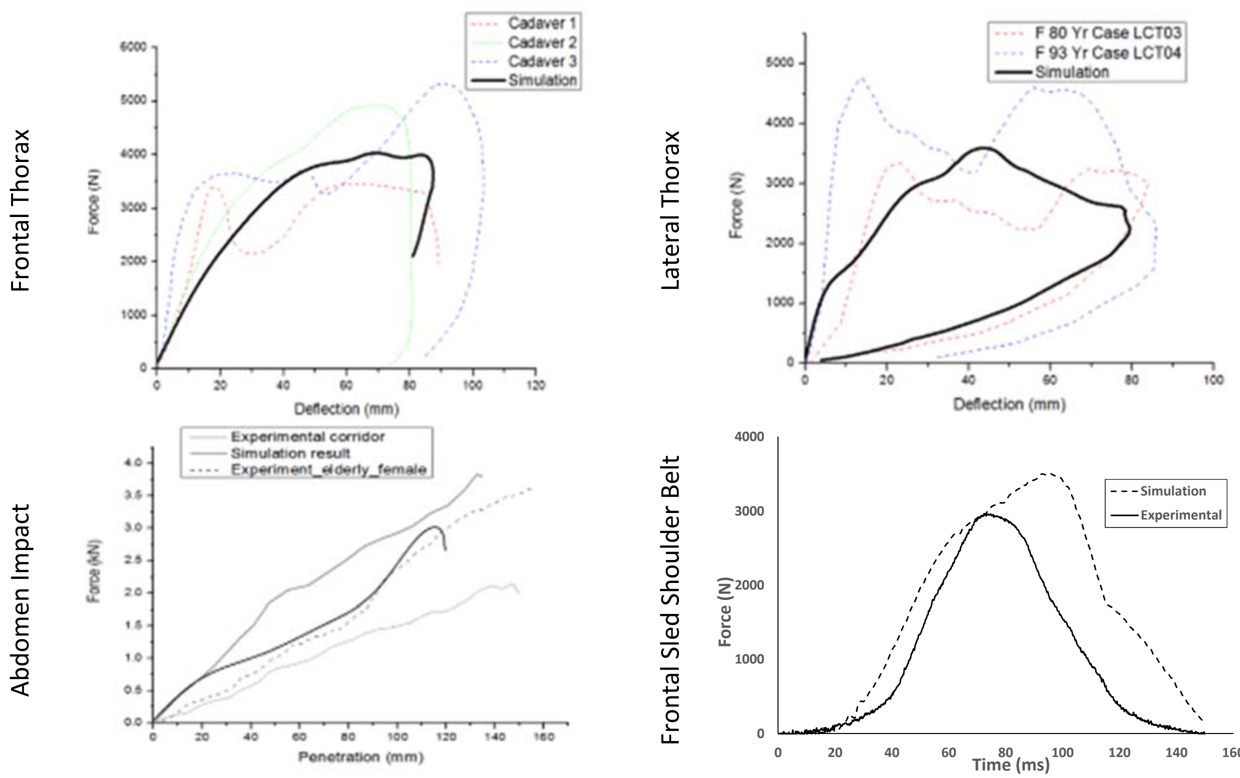

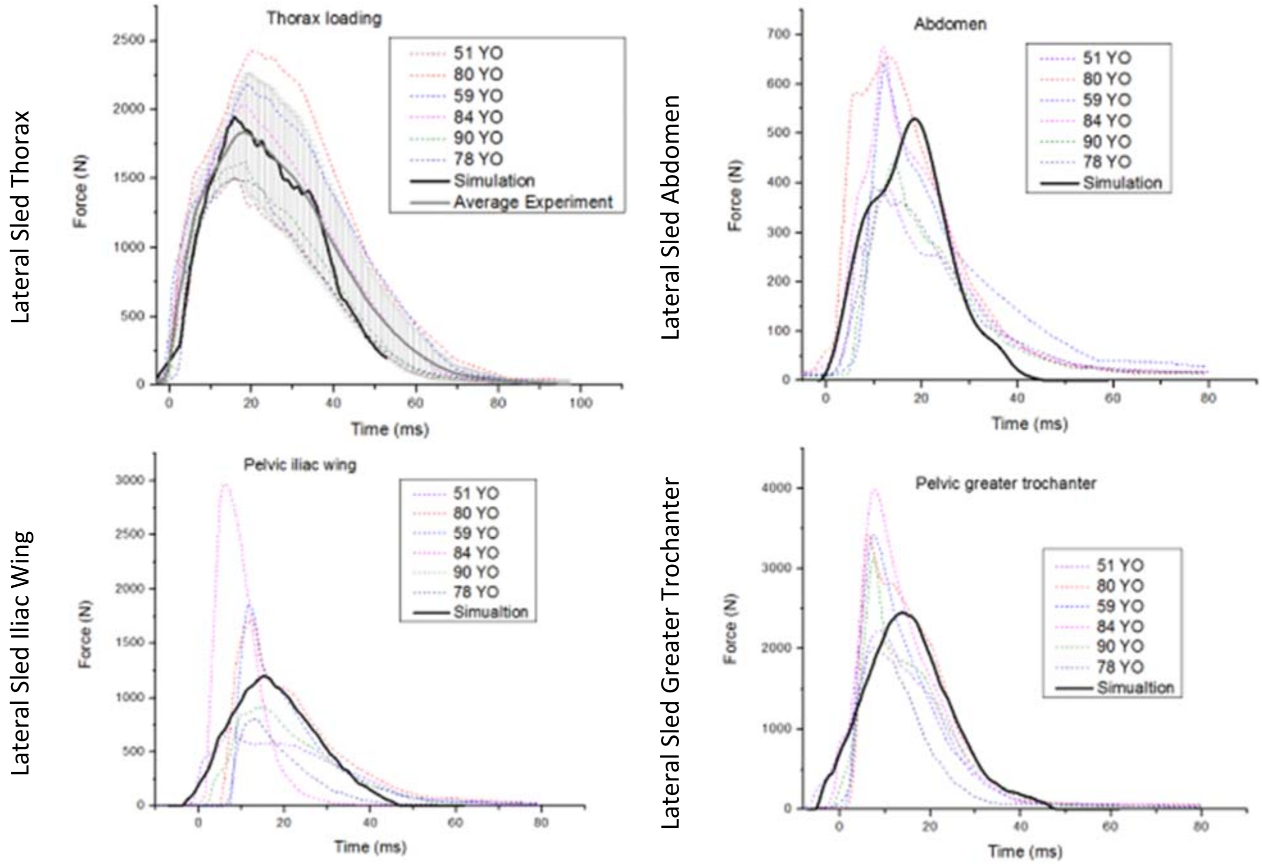

Fig. 4. Simulation results plotted against experimental data for elderly female cases.

A summary of the ISO/TS 18571 scores is presented in Table IV. The total ISO/TS 18571 rating ranged from 0.62 to 0.81. Overall, the magnitude was the best scores for all the validations. All the whole-body level validations are in fair or good agreement with the experimental results.

TABLE IV
ISO SCORES FOR WHOLE-BODY LEVEL VALIDATIONS

Simulation	Signal	Corridor	Phase	Magnitude	Slope	ISO Score
Thorax lateral impact	Force vs deflection	0.73	0.93	0.94	0.70	0.81
Thorax frontal impact	Force vs deflection	0.71	0.68	0.92	0.66	0.74
Abdominal impact	Force vs deflection	0.83	0.51	0.77	0.62	0.71
Frontal sled test	Shoulder-belt force vs time	0.54	0.65	0.82	0.55	0.62
Lateral sled test	Force vs time at thorax	0.63	0.31	0.92	0.81	0.66
	Force vs time at abdomen	0.86	0.80	0.84	0.52	0.78
	Force vs time at pelvic iliac wing	0.66	0.83	0.81	0.79	0.75
	Force vs time at pelvic greater trochanter	0.59	0.66	0.75	0.63	0.64

The model-predicted rib fractures for the whole-body level validations are compared with experimental results in Table V. In general, the CHARM-70F model can predict similar number of rib fractures generated by elderly female occupants in the validation cases.

TABLE V
RIB FRACTURE PREDICTION FOR THE CHARM-70F COMPARED TO EXPERIMENTAL INJURY REPORTS

Experiment	**Sample Size (N)**	**Average Number of Rib Fractures during Tests**	**Number of Rib Fractures Predicted by CHARM-70F**
Frontal Thorax Impact	3	13	11
Lateral Thorax Impact*	2	17	11
Frontal Sled	1	1	1
Lateral Sled	4	3	3

* The lateral thorax impact study by Talantikite *et al.* [30] also reported an average number of fractured ribs of 7.5, while CHARM-70F predicted 5 fractured ribs.

IV. DISCUSSION

In this study, detailed FE whole-body models were developed for the average elderly female. PMHS CT scans provided details for the bony structures. Statistical average geometry of the body surface and ribcage were incorporated to ensure the final anthropometry accurately represented the 50th percentile population. In the model validation process, both component and whole-body level validations were applied. The experimental data were selected carefully so that the simulation results could compare directly with data of elderly female PHMS. Direct comparison with elderly female PMHS data reduced the potential errors introduced from scaling methods.

Through quantitative evaluation, the CHARM-70F model showed fair to good agreement with the experimental results. The ISO score ranges from 0.62 to 0.81. At the current stage, only whole-body level validation responses were quantitatively evaluated. Future work will apply the ISO score rating to all component level validations. Besides comparison of the force time history, bone fractures, especially rib fractures, were tracked against the validation results where fracture was reported. From the summary of Table V, the predicted number of rib fractures can generally reflect the reported quantity of rib fractures in the validation cases.

To represent an average geometry of rib cage for an elderly female, the statistical model developed by Shi et al. [18] was applied to finalize our rib cage geometry. Recently, Holcombe et al. [10] published their study on developing the statistical model of rib geometry. Both models account for parameters such as age, gender, height, and BMI and can easily generate rib geometry by inputting control parameters. Holcombe's model is better in defining detailed rib geometry. Shi's model defines the whole rib cage geometry with one model so it also defines the relative position among ribs. In addition, Shi's model gives information regarding the rib cross-section geometry along the length of the rib structure. A future study can be performed to compare the geometry difference, if there is any, generated by these two statistical models.

Thorax modeling and rib fracture prediction are the major tasks for modeling of the elderly population. Antona-Makoshi's study [14] obtained the material parameters for elderly ribs through an optimization strategy. Scaling law was applied to define the material properties for younger setting. From this study, the Young's modulus, yielding stress, and ultimate strain of elderly rib cortical bone were defined as 12 GPa, 0.1 GPa, and 1.2% (calculation for data points captured from the stress-strain plots). Schoell's study [15] obtained the rib material properties for elderly by applying the age-dependent scaling law to the material parameters defined in the GHBMC M50. The Young's modulus, yielding stress, and ultimate strain for elderly rib cortical bone were reported as 11.5 GPa, 0.088 GPa, and 2.03%. In the current study, material properties for rib cortical bones were obtained from an optimization method by Kalra [22]. The Young's modulus, yielding stress, and ultimate strain were defined as 9.8 GPa, 0.097 GPa, and 1.4%. Overall, the reported material properties for elderly rib cortical bone from these studies correlated to each other. A relatively lower Young's modulus was reported in the current study. Whether this difference was caused by gender or other factors, such as bone mineral density, is not clear and may need further studies.

The major limitation of this study was the relatively small sample size. This strategy of direct comparison with elderly female PMHS data narrowed the availability of data source and made it relatively hard to find enough data sample size to compare the simulation results with a testing corridor. As a result, the selected frontal sled test is not good for validation purposes. There were too many uncertain parameters in the experimental setups that were not well documented in the literature. That brought difficulties in defining loading and boundary conditions for modeling and undermined the validity of the simulation results. We will continue our validation efforts if more suitable data can be recruited in the future.

V. CONCLUSIONS

In this study, the CHARM-70F finite element model was developed to represent the 50th percentile elderly females of 60–80 years of age. Model validation was performed at both component and whole-body levels. Simulation results were directly compared with elderly female PMHS data reported from the literature. The ISO/TS 18571 score was calculated to quantitatively evaluate the model performance. Overall, the model was found to be computationally stable under validated loading conditions and showed fair to good agreement with the experimental results presented in the literature. Further improvement of the model biofidelity can be achieved if more population-specific material properties and injury tolerances are revealed in the future.

VI. ACKNOWLEDGEMENTS

This study is financially supported by Toyota's Collaborative Safety Research Center (CSRC, Saline, MI). Authors would like to gratefully acknowledge Dr Jingwen Hu from UMTRI, Dr Richard Kent from University of Virginia, and Dr Ashley Weaver from Wake Forest University for their data support throughout the model developing and validation processes.

VII. REFERENCES

[1] NHTSA. (2013) Injury Vulnerability and Effectiveness of occupant protection technologies for older occupants and women. DOT HS 811 766.

[2] Lenard, J., Welsh, R. (2001) A comparison of injury risk and pattern of injury for male and female occupants of moden European passenger cars. *Proceedings of IRCOBI Conference*, 2001, Isle of Man.

[3] Roberts, V. L. and Compton, C. (1993) The relationship between Delta V and injury. *SAE Technical Paper,* 933111.

[4] Bose, D., Segui-Gomez, M., Crandall, J. R. (2011) Vulnerability of female drivers involved in motor vehicle crashes: an analysis of US population at risk. *American journal of public health,* **101**(12): pp.2368–73.

[5] Wang, S. (2008) "Elderly occupants: Injury risks and pattern". Internet: http://crashedu.org/articulate/elderly_ed/Part1/player.html. Accessed on 4/7/2018.

[6] Kent, R., *et al*. (2005) Structural and material changes in the aging thorax and their role in crash protection for older occupants. *Stapp Car Crash Journal,* **49**: pp. 231–49.

[7] Bellemare, F., Jeanneret, A., Couture, J. (2003) Sex Differences in Thoracic Dimensions and Configuration. *American Journal of Respiratory and Critical Care Medicine*, **168**(3): pp. 305–12.

[8] Gayzik, F. S., Yu, M. M., Danelson, K. A., Slice, D. E., Stitzel, J. D. (2008) Quantification of age-related shape change of the human rib cage through geometric morphometrics. *Journal of Biomechanics*, **41**(7): pp. 1545–54

[9] Kalra, A., *et al*. (2015) Characterization of Human Rib Biomechanical Responses due to Three-Point Bending. *Stapp Car Crash Journal*, **59**: pp. 113–30.

[10] Holcombe, S. A., Wang, S. C., Grotberg, J. B. (2017) The effect of age and demographics on rib shape. *Journal of Anatomy*, **231**(2): pp.229-47.

[11] Nalla, R. K., Kruzic, J. J., Kinney, J. H., Ritchie, R. O. (2004) Effect of aging on the toughness of human cortical bone: evaluation by R-curves. *Bone,* **35**(6): pp. 1240–46.

[12] Riggs, B. L., Melton, I. L. J. III, Robb, R. A., Camp, J. J., Atkinson, E. J. (2004) Population-based study of age and sex differences in bone volumetric density, size, geometry, and structure at different skeletal sites. *Journal of Bone and Mineral Research.,* **19**(12): pp. 1945–54.

[13] Iwamoto, M., Nakahira, Y., Kimpara, H., Min, K. (2013) Development of a Finite Element Model of 5th Percentile Female with Multiple Muscles and Its Application to Investigation on Impact Responses of Elderly Females. *23rd International Technical Conference on the Enhanced Safety of Vehicles (ESV),* 2013, Seoul, Republic of Korea.

[14] Antona-Makoshi, J. *et al*. (2015) Age-Dependent Factors Affecting Thoracic Response: A Finite Element Study Focused on Japanese Elderly Occupants. *Traffic Injury Prevention*, **16**:sup1, S66-S74.

[15] Schoell, S. L. *et al.* (2015) Development and Validation of an Older Occupant Finite Element Model of a Mid-Sized Male for Investigation of Age-Related Injury Risk. *Stapp Car Crash Journal*, 59: pp. 359-83.

[16] Fryar, C. D., Gu, Q., Ogden, C. L., Flegal, K. M. (2016) Anthropometric reference data for children and adults: United States, 2011-2014. *Vital Health Statistics,* **3**(39).

[17] Reed, M. P., Ebert, S. M., Hallman, J. J. (2013) Effects of driver characteristics on seat belt fit. *Stapp Car Crash Journal*, **57**: pp. 43–57.

[18] Shi, X., *et al*. (2014) A statistical human rib cage geometry model accounting for variations by age, sex, stature and body mass index. *Journal of biomechanics*, **47**(10): pp.2277–85.

[19] Li, Z., Kinding, M. W., Kent, R. (2010) Development of a Finite Element Ribcage Model of the 50th Percentile Male with Variable Rib Cortical Thickness. *39th International workshop on Injury Biomechanics research,* 2010, Detroit, USA.

[20] Mohr, M., Abrams, E., Engel, C., Long, W. B., Bottlang, M. (2007) Geometry of human ribs pertinent to orthopedic chest-wall reconstruction. *Journal of Biomechanics,* **40**(6): pp. 1310–17.

[21] Weaver, A. A., Schoell, S. L. Stitzel, J. D. (2014) Morphometric analysis of variation in the ribs with age and sex. *Journal of Anatomy,* **225**(2): pp. 246–61.

[22] Kalra, A. (2017) Development of an elderly female torso finite element model for restraint system research and development applications. Doctoral thesis. Wayne State University.

[23] Nahum, A. M., Smith, R., Ward, C. C. (1977) Intracranial pressure dynamics during head impact. SAE Technical Paper.

[24] Allsop, D. (1988) Facial impact response: A comparison of the hybrid III dummy and human cadaver. *Stapp Car Crash Journal*, pp. 139–55.

[25] Hardy, W., Foster, C. D., Mason, M. J., Yang, K. H., King, A. I. (2007) Investigation of head injury mechanisms using neutral density technology and high-speed biplanar X-ray. *Stapp Car Crash Journal*, **45**: pp. 337–68.

[26] Nightingale, R. W., McElhaney, J. H., Richardson, W. J., Myers, B. S. (1996) Dynamic responses of the head and cervical spine to axial impact loading. *Journal of Biomechanics*, **29**(3): pp. 307–18.

[27] Deng, B., Begeman, P. C., Yang, K. H., Tashman, S., King, A. I. (2000) Kinematics of human cadaver cervical spine during low speed rear-end impacts. *Stapp Car Crash Journal*, **44**: pp. 171–88.

[28] Vezin, P. and Berthet, F. (2009) Structural characterization of human rib cage behavior under dynamic loading. *Stapp Car Crash Journal*, **53**: pp. 93–125.

[29] Kroell, C. K., Schneider, D. C., and Nahum A.M. (1971) Impact Tolerance and Response of the Human Thorax. SAE Technical Paper.

[30] Talantikite, Y., *et al*. (1998) Human thorax behaviour for side impact-Influence of impact mass and velocities. *16th Conference on the Enhanced Safety of Vehicles*, 1998, Windsor, Canada.

[31] Guillemot, H., Besnault, B., Robin, S., Got, C., Le Coz, J. (1997) Pelvis Injuries in Side Impact Collisions : A Field Accident Analysis and Dynamic Tests on Isolated Pelvis Bones. in SAE Technical Paper.

[32] Cavanaugh, J. M., Nyquist, G. W., Goldberg, S. J., King, A. I. (1986) Lower abdominal tolerance and response. SAE Technjical Paper.

[33] Ramet, D. and Cesari, D. (1979) Experimental study of pelvis tolerance in lateral impact. *International IRCOBI Conference on the Biomechanics of Impacts*, 1979, Göteborg, Sweden.

[34] Demetropoulos, C. K., Yang, K. H., Grimm, M. J., Khalil, T. B., King, A. I. (1998) Mechanical properties of the cadaveric and Hybrid III lumbar spines. SAE Technical Paper.

[35] Kerrigan, J. R., *et al*. (2003) Experiments for Establishing Pedestrian-Impact Lower Limb Injury Criteria. SAE World Congress and Exhibition, 2003, Warrendale, USA.

[36] Viano, D. C., Culver, C. C., Haut, R. C., Melvin, J. W., Bender, M. (1978) Bolster impacts to the knee and tibia of human cadavers and an anthropomorphic dummy. SAE Technical Paper.

[37] Rupp, J. D., Reed, M. P., Van Ee, C. A., Kuppa, S., Wang, S. C. (2002) The tolerance of the human hip to dynamic knee loading. *Stapp Car Crash Journal*, **46**: pp. 211–28.

[38] Duma, S. M., *et al*. (1999) Dynamic injury tolerances for long bones of the female upper extremity. *Journal of Anatomy*, **194**(3): pp. 463–71.

[39] Petitjean, A., Lebarbe, M., Potier, P., Trosseille, X., Lassau, J. P. (2002) Laboratory Reconstruction of real world frontal crash configuration using the Hybrid III and THOR Dummies and PMHS. *Stapp Car Crash Journal*, **46**.

[40] Wood, L. K., Miller, C. S., Madura, N. H., Reed, M. P., Schneider, L. W. (2014) Response and Tolerance of Female and/or Elderly PMHS to Lateral Impact. *Stapp Car Crash Journal*, **58**: pp. 523–63.

VIII. APPENDIX

Appendix A: Material Properties Defined in CHARM-70F Model

TABLE A1
SUMMARY OF THE MATERIAL PROPERTIES USED IN THE HEAD MODEL

Component	Material model	Material parameters	Failure criterion
Outer Skin	Elastic	ρ=1.1e-06 kg/mm^3, γ= 0.45, E= 0.01 GPa	-
Neck Flesh	Soft tissue with viscosity	ρ=1.0e-06 kg/mm^3, Bulk =0.1 GPa Mooney-Rivlin parameters: C_1=C_2= 9e-5 GPa	-
Maxilla	Piecewise linear plastic	ρ=2.1e-06 kg/mm^3, γ=0.25, E=3.0 GPa, σ_Y=0.4 GPa	ε_{max} =0.0091
Forehead	Simplified rubber/foam	ρ=1.0e-06 kg/mm^3, γ=0.35, Bulk =0.1 GPa	-
Brain	Viscoelastic	ρ=1.0e-06 kg/mm^3, G_0=6e-6 GPa, G_t =5e-7 GPa, Bulk =2.19 GPa	
Skull	Elastic	ρ=2.1e-06 kg/mm^3, γ=0.45, E = 10 GPa	
Sinus	Elastic	ρ=1.0e-06 kg/mm^3, γ=0.3, E = 0.001 GPa	
Falx, Pia	Elastic	ρ=1.0e-06 kg/mm^3, γ=0.35, E = 0.0125 GPa	

ρ, density; E, Young's modulus; γ, Poisson's ratio; σ_Y, yield strength

TABLE A2
SUMMARY OF THE MATERIAL PROPERTIES OF PARTS IN THE NECK MODEL

Part	Material law	Material parameters
Cancellous bone	Power law plasticity	ρ =1.09e-006 kg/mm^3, E=0.291 GPa, γ =0.3, k=0.007118, N=0.2741
Cortical bone	Plastic kinematics	ρ =2e-006 kg/mm^3, E=16.8 GPa, γ =0.3
Disc	Simplified rubber/foam	ρ =1.36e-006 kg/mm^3, km=1.72
Nucleus	Hill Foam	ρ =1.36e-006 kg/mm^3, K=1, N=2, MU=0.1
Muscles	Mat_Muscle	Active response is disabled, passive properties defined with curves

Where ρ, density; E= Young's modulus; γ =Poisson's ratio; k= strength coefficient; N= hardening coefficient; km= Linear bulk modulus; MU= Damping coefficient.

TABLE A3
SUMMARY OF THE MATERIAL PROPERTIES OF PARTS IN THE THORAX ASSEMBLY MODEL

Part	Material law	Material constants
Vertebrae cancellous bone	Elastic-Plastic	ρ =1.0e-006 kg/mm^3, E=0.04 GPa, σ_y =0.002 GPa, E_{tan}=0.01 GPa,
Vertebrae cortical bone	Elastic-Plastic	ρ =1.8e-006 kg/mm^3, E=9.8 GPa, σ_y =0.08 GPa, E_{tan}=1.35 GPa,
Rib cancellous bone	Elastic-Plastic	E=0.04 GPa, σ_y =0.002 GPa, E_{tan}=0.01 GPa,
Rib cortical bone	Elastic-Plastic	E=9.8 GPa, σ_y =0.097 GPa, E_{tan}=1.35 GPa, Plastic failure strain: 0.14
Thoracic disc	Elastic	ρ =1.1e-006 kg/mm^3, E=0.0364 GPa, γ =0.4
Aorta, intercostal muscle, veins	Elastic	ρ =1.2e-006 kg/mm^3, E=0.001 GPa, γ =0.45
Cartilage	Elastic	ρ =1.1e-006 kg/mm^3, E=0.05 GPa, γ =0.35
Pancreas	Elastic	ρ =1.1e-006 kg/mm^3, E=0.03 GPa, γ =0.45
Clavicle ligaments	Elastic	ρ =1.1e-006 kg/mm^3, E=0.104 GPa, γ =0.45
Stomach	Elastic fluid	ρ =1.0e-006 kg/mm^3, Bulk =1.4 GPa
Gallbladder	Elastic fluid	ρ =1.0e-006 kg/mm^3, Bulk =2.2 GPa
Blood	Elastic fluid	ρ =1.0e-006 kg/mm^3, Bulk =2.2 GPa
Lung	Elastic fluid	ρ =1.0e-006 kg/mm^3, Bulk = 1.4 GPa
Heart	Heart tissue	ρ=1.0e-06 kg/mm^3, P = 3.48 GPa

Spleen	Viscous foam	ρ=1.1e-06 kg/mm^3, E_i = 9.8e-5 GPa, E_v=0.0085, γ =0.45
Liver	Viscoelastic	ρ=6.0e-07 kg/mm^3, G_0=2.3e-4 GPa, G_t =4.3e-5 GPa, Bulk=2.87e-3 GPa, beta=0.635
Soft tissue filling	Soft tissue	ρ=1.1e-06 kg/mm^3, C_1= 7.2e-6 GPa, C_2=8.5e-6 GPa, Bulk = 0.01GPa
Flesh	Simplified rubber/foam	ρ=1.06e-06 kg/mm^3, damping coefficient = 0.1 Bulk = 0.5 GPa, stress-strain curve
Intestine	Elastic	ρ =1.1e-006 kg/mm^3, E=0.03 GPa, γ =0.45
Humerus trabecular	Elastic plastic	ρ =1.0e-006 kg/mm^3, E=0.001 GPa, σ_y =0.07 GPa
Humerus cortical	Elastic plastic	ρ =1.8e-006 kg/mm^3, E=14 GPa, σ_y =0.1 GPa

Where ρ, density; E= young's modulus; γ =poisson's ratio; C_1, C_2 = hyper elastic coefficients, G_0 = short term shear modulus, G_t = long term shear modulus, P = Pressure, Ei=Initial young modulus, Ev= Viscous young modulus, σ_y = Yield stress, E_{tan} = Tangent modulus.

TABLE A4
SUMMARY OF THE MATERIAL PROPERTIES OF PARTS IN THE LUMBAR MODEL

Components	**Material Model**	**Young's Modulus (GPa)**	**Poisson's ratio**
Vertebral cortical bone	Elastic	12	0.3
Vertebral trabecular bone	Elastic	0.100	0.2
Posterior cortical bone	Elastic	12	0.3
Posterior trabecular bone	Elastic	3.5	0.25
Nucleus pulposus	Incompressible, elastic fluid	0.001	0.499
Fiber of annulus	4-layers fabric	0.357-0.550	0.3
Endplates	elastic	0.023	0.4

TABLE A5
SUMMARY OF THE MATERIAL PROPERTIES OF PARTS IN THE PELVIS AND LOWER EXTREMITY

Component	**Material model**	**Material parameters**	**Failure criterion**
Cortical at long bones	Piecewise linear plastic	ρ=2e-6 kg/mm^3, γ=0.3, E=17 GPa. σ_Y=134 MPa	ε_{max} =0.01
Cortical at pelvis	Piecewise linear plastic	ρ=2e-6 kg/mm^3, γ=0.29, E=17 GPa, σ_Y=800 MPa	ε_{max} =0.02
Trabecular at long bones	Plastic kinematics	ρ=1.1 e-6 kg/mm^3, γ=0.3, E=0.44 GPa. σ_Y=9MPa – 2.5MPa (Femur Head) and 5.3 MPa (Femur End)	-
Trabecular at pelvis	Piecewise linear plastic	ρ=1.6 e-6 kg/mm^3, γ=0.3, E=0.07GPa, σ_Y=10Mpa	ε_{max} =0.022
SI joint &socket cartilage	Hyperelastic	ρ=1.6 e-6 kg/mm^3, γ=0.495 Mooney-Rivlin parameters: C_{10}=0.05 MPa, C_{01}=0.2 MPa, C_{11}=0.25 MPa	-
Knee ligaments	Elastic	ρ=1.1 e-6 kg/mm^3, γ=0.22 E=0.345 GPa, σ_Y=29.8 MPa	-
Pelvis ligaments	Discrete beam	Hip joint (53 beams each side) ρ=1.2 e-6 kg/mm^3, E= 250 MPa	-
Flesh for pelvis	Soft tissue	ρ=0.73 e-6 kg/mm^3, $Bulk$=20 MPa Mooney-Rivlin parameters: C_1=C_2= 10 kPa	-
Flesh for limbs	Soft tissue	ρ=1.3 e-6 kg/mm^3 Mooney-Rivlin parameters: C_1=C_2= 10 kPa	-

Where ρ, density; E, Young's modulus; γ, Poisson's ratio; σ_Y, yield strength.

Appendix B: Component Level Validations

Brain intracranial pressure

Linear acceleration was applied to the head at 45° inclination with respect to the Frankfort anatomical plane, according to Nahum's study [19]. Intracranial pressures were measured at frontal, parietal, occipital and posterior locations (Fig. B1).

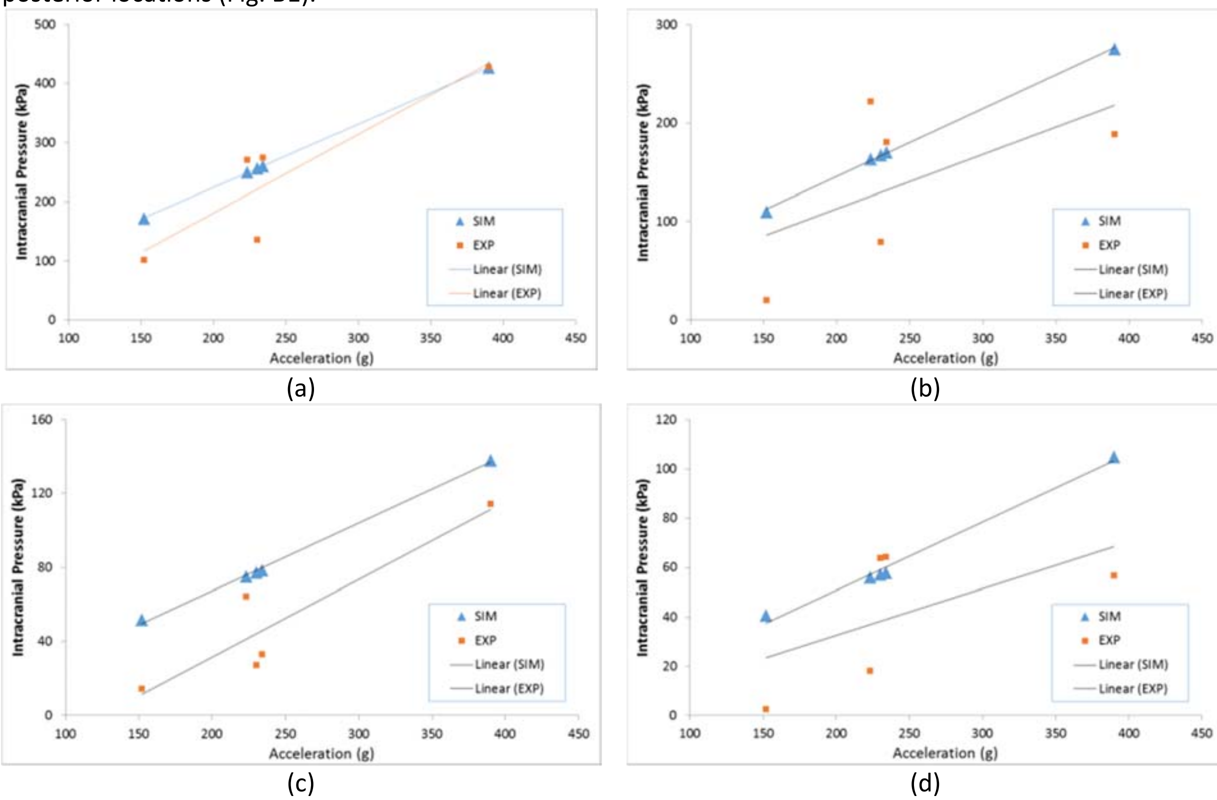

Fig. B1. Intracranial Pressure simulation (blue) and experimental (orange) results with linear regression lines at (a) frontal, (b) parietal, (c) occipital and (d) posterior locations.

Brain-skull relative motion

Validation on brain-skull relative motion was performed based on Hardy *et al.* [21]. Linear and rotational accelerations along the x, y and z directions at CG of head were applied. The relative displacements of the brain with respect to the skull were compared with the test results from elderly female cadavers, as shown in Fig. B2.

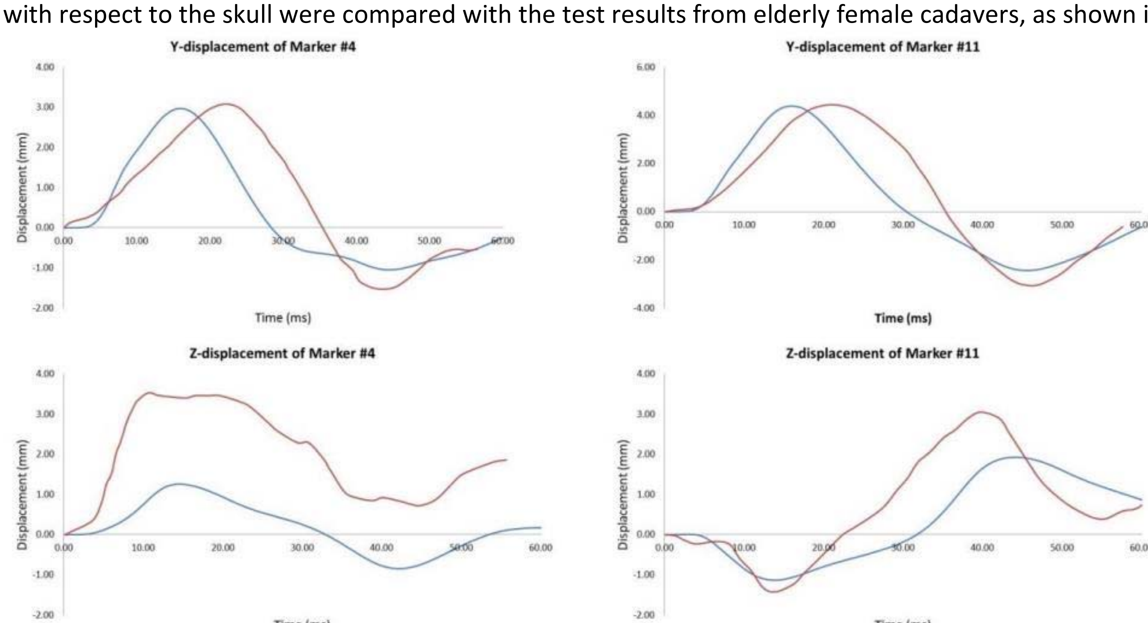

Fig. B2-1. Simulation (blue) and experimental (orange) data of brain-skull relative motion for test 380-T3.

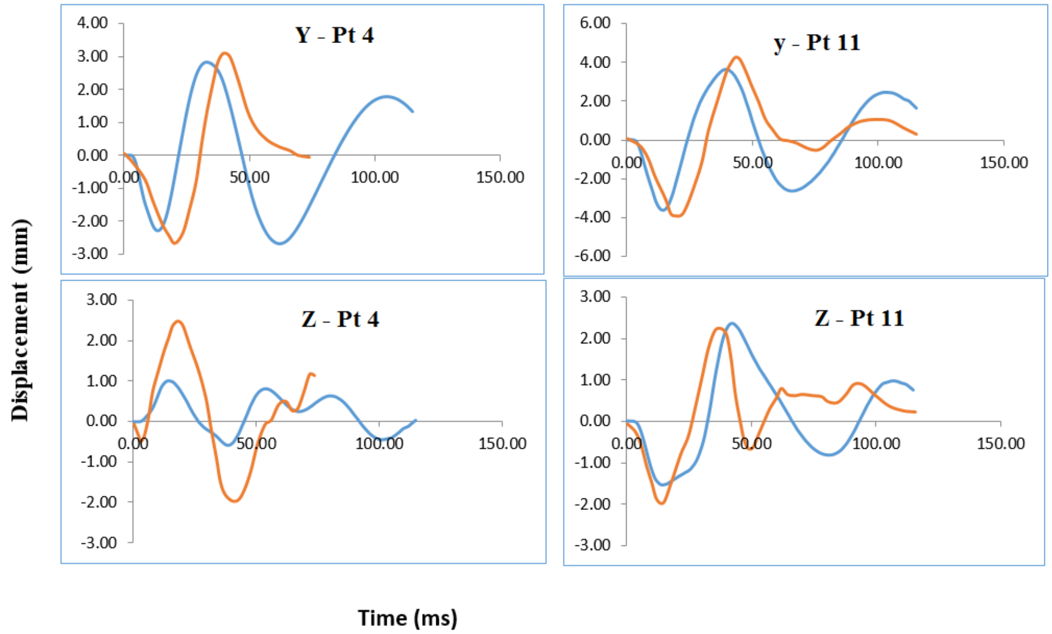

Fig. B2-2. Comparison of brain-skull relative motion for simulation and experiment for Case-380 T1 (Blue-Simulation, Orange-Experiment).

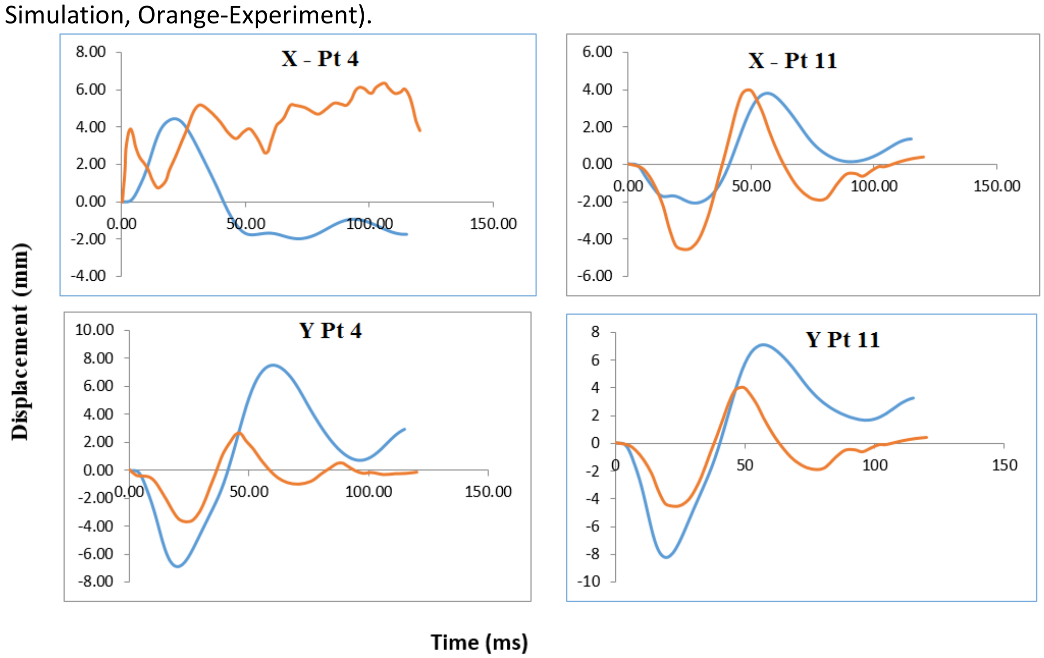

Fig. B2-3. Comparison of brain-skull relative motion for simulation and experiment for C380-T2 (Blue-Simulation, Orange-Experiment).

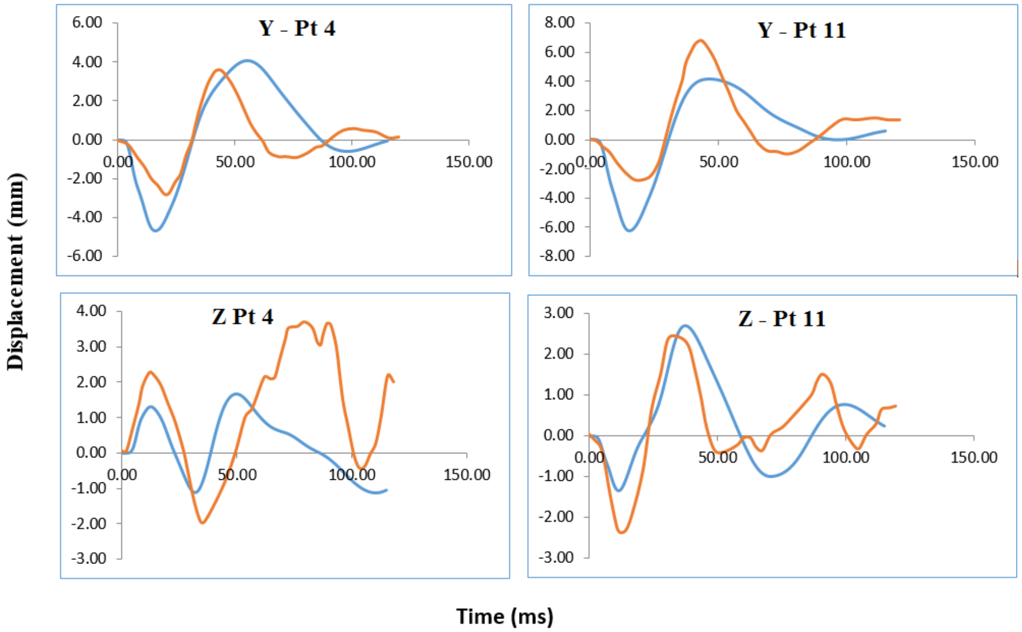

Fig. B2-4. Comparison of brain-skull relative motion for simulation and experiment for Case-380 T6 (Blue-Simulation, Orange-Experiment).

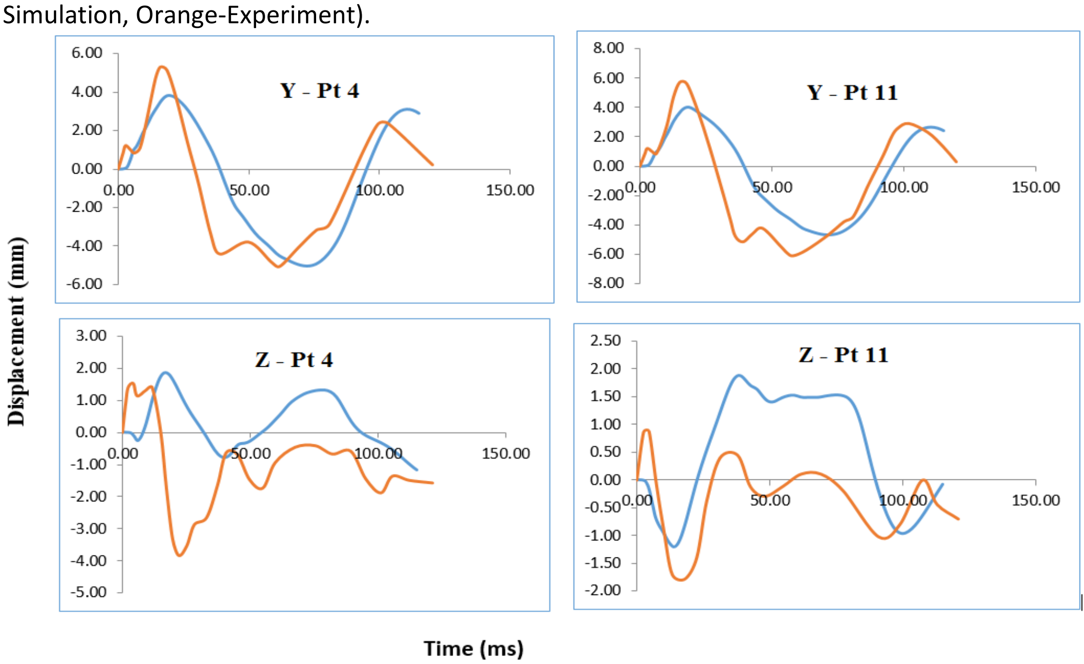

Fig. B2-5. Comparison of brain-skull relative motion for simulation and experiment for Case-393 (Blue-Simulation, Orange-Experiment).

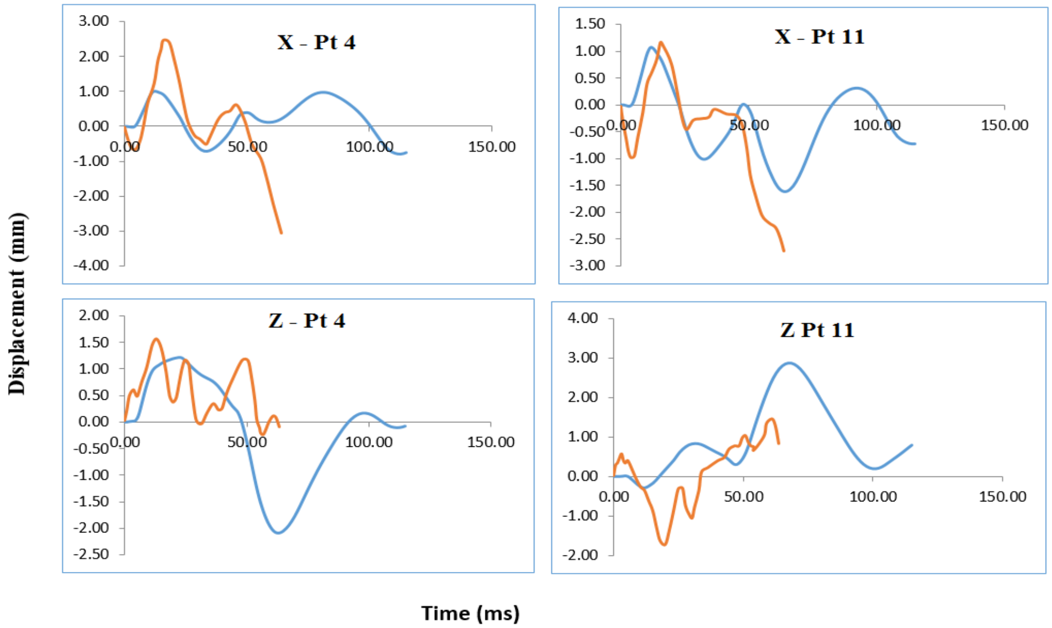

Fig. B2-6. Comparison of brain-skull relative motion for simulation and experiment for Case-288 T1 (Blue-Simulation, Orange-Experiment).

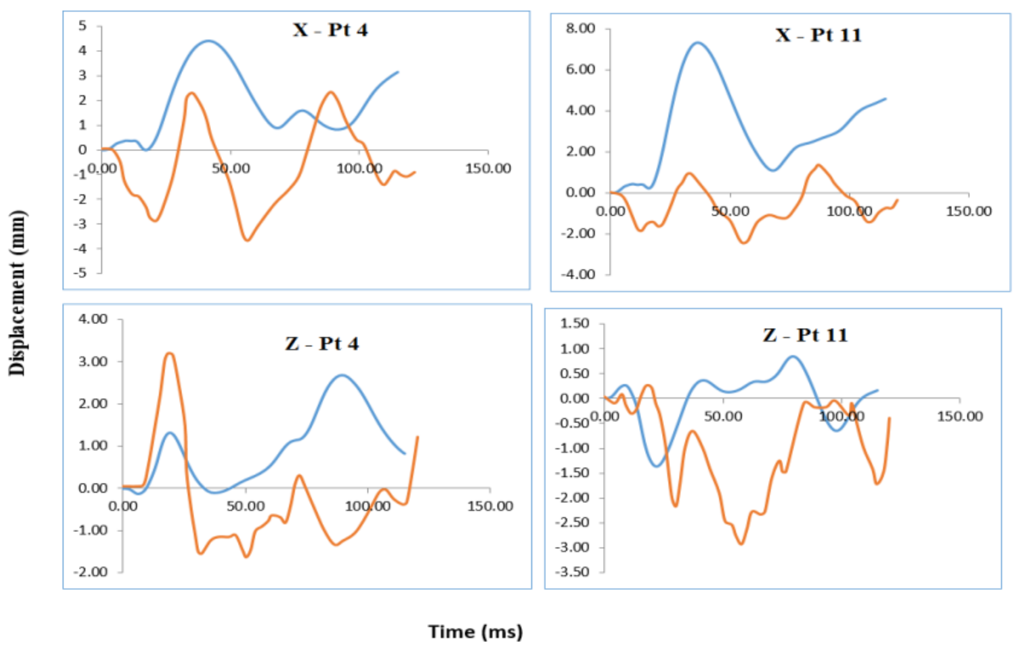

Fig. B2-7. Comparison of brain-skull relative motion for simulation and experiment for Case-288 T2 (Blue-Simulation, Orange-Experiment).

Facial bone impact

Rigid bar impacts on the maxilla, zygoma and frontal region were simulated based on Allsop's study [20]. The total weight of the impactor was 14.5 kg and the average loading speed was 3.0 m/s. The force-deflection histories for elderly female PMHS tests were retrieved and the corresponding corridors were generated for each impact location with mean ± standard deviation (SD). The model-predicted responses were plotted together with the developed corridor, as shown in Fig. B3.

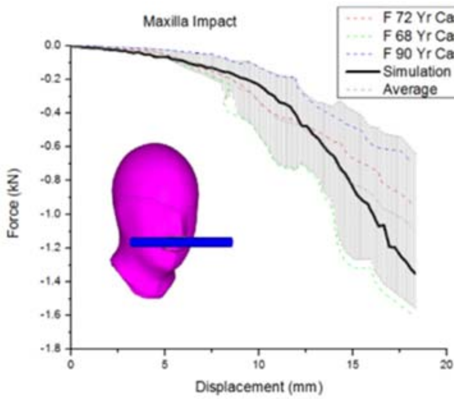

(a)

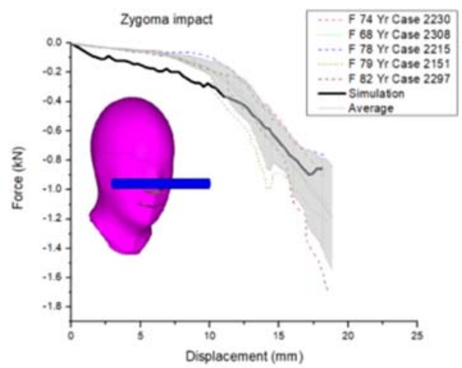

(b)

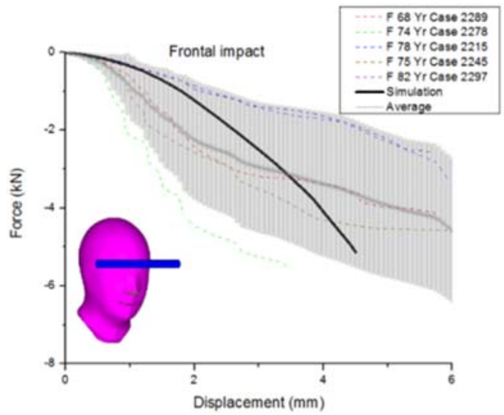

(c)

Fig. B3. Comparison of force-deflection for facial impact responses at (a) maxilla, (b) zygoma and (c) frontal bone.

Whiplash loading

The CHARM-70F neck response under whiplash loading was performed based on a rear-end impact sled test conducted by Deng *et al.* [23]. Kinematics of T1 was defined as input and the resultant head kinematics and rotation history with respect to the neck were compared with experimental data, as shown in Fig. B4.

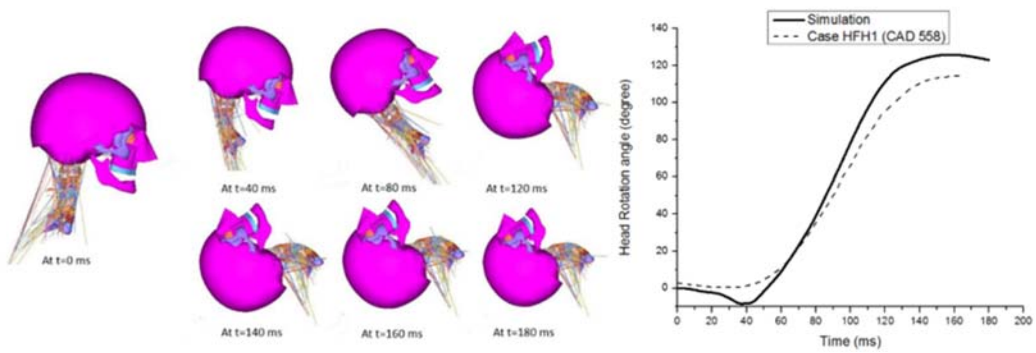

Fig. B4. Simulated response sequence of rear-end impact loading and comparison of head rotation history.

Neck Axial Compression

Nightingale *et al*. (1997) conducted head impact experiments using head and neck complexes taken from 22 cadavers. These tests were conducted on a drop track system to produce impact velocity in the range of 3.2 m/s on the padded and rigid surfaces. An effective torso mass of 16 kg (based on GEBOD output for a 50th percentile male) was simulated in the experiment using a steel carriage. The head impact forces occurred due to the drop were recorded at the T1 junction. Out of 22 cadaveric specimens, only two cadavers were of elderly female (age > 60yo), the force–time history related to these two cadavers (63yo and 75yo) were considered for model validation from test no I11-P+15 and N02-P+0, respectively. Both tests were carried out using a padded surface, which was simulated using a foam material in the simulation. The simulation response from 10 m/s to 60 m/s and the corresponding comparison of the force-time history for these two tests is shown in Fig. B5.

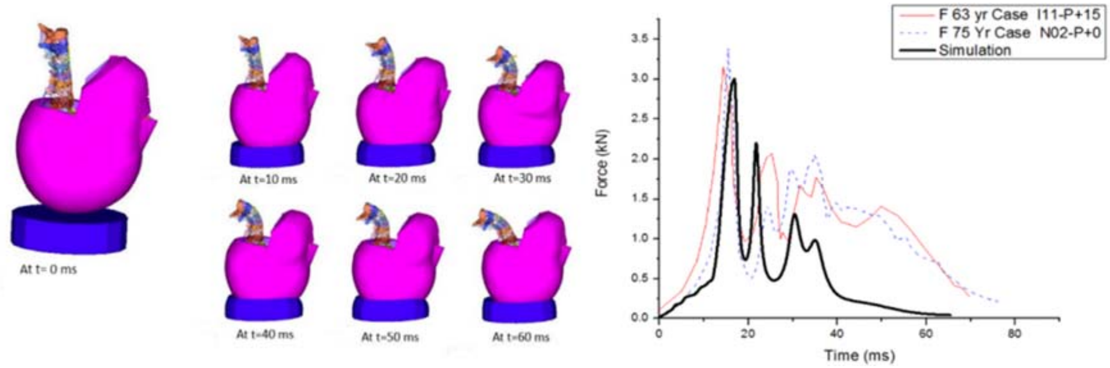

Fig. B5. Simulation responses at different time intervals and comparison of simulation and experimental results for the simulated drop test.

Isolated ribcage loading

The overall behaviour for the stiffness of the costovertebral joints, as well as the ribcage, was validated against experimental data reported by Vezin and Bethet (2009), as shown in Fig. B6(a). The ribcage model was loaded using the displacement profile reported in the experiment, with a peak velocity Vmax of 1.67 m/s. The deformed ribcage shape and the corresponding force and deflection characteristics of each specimen were retrieved for the FE model validation, as shown in Figs B6 (b) and (c), respectively.

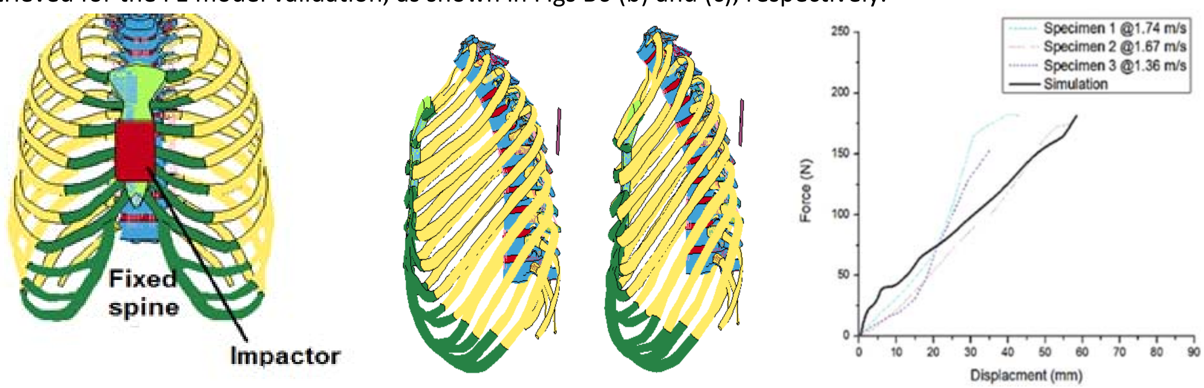

(a) (b) (c)

Fig. B6. (a) Simulation setup, (b) deformation of the ribcage before (left) and after (right) impact, and (c) comparison between experiment and simulation force deflection curves.

Table top thorax impact

Kent *et al*. [6] performed thoracic impact tests for hub loading and belt loading in different configurations (diagonal, double diagonal and distributed) conditions on 15 human cadaver specimens. Out of these specimens, six specimens were of elderly female with ages from 60yo to 80yo. The data presented in the publication was scaled to the 50th percentile male, but the original data related to the six elderly female cadavers were kindly provided by the authors through personal communication. The prescribed motion was added at the end of seat-belt elements to mimic the exact loading condition as in experiment. Figure B7 shows the simulation setups for all loading conditions. A constant gravitational load was applied to the model so that it can initiate the proper contact with posterior loading plate for a total of 150 m/s.

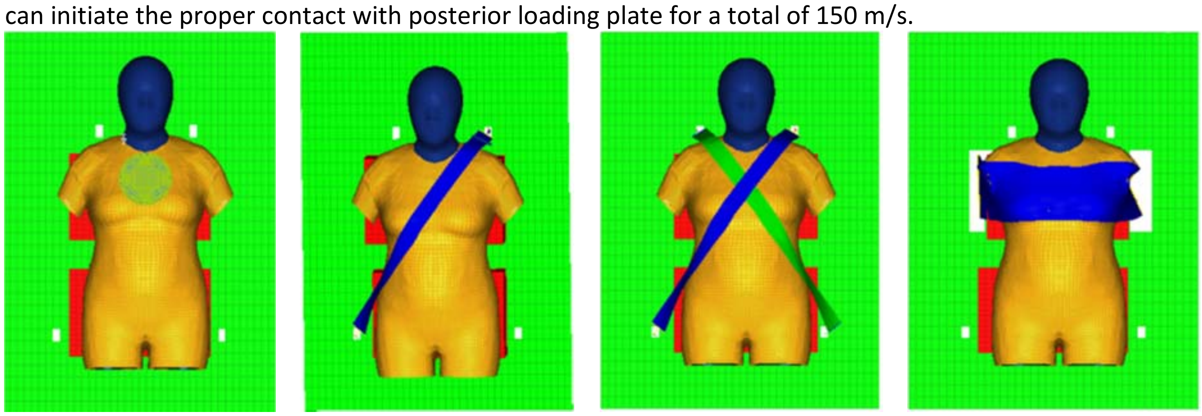

(a) (b) (c) (d)

Fig. B7. Simulation setups of (a) hub loading, (b) diagonal belt, (c) double diagonal belt and (d) distributed belt for table top thorax impact experiments.

The comparison of force versus deflection for the experimental and simulation results is shown in Fig. B8. Only responses related to female cadavers with ages greater than 60yo were chosen from the experimental data for model comparison.

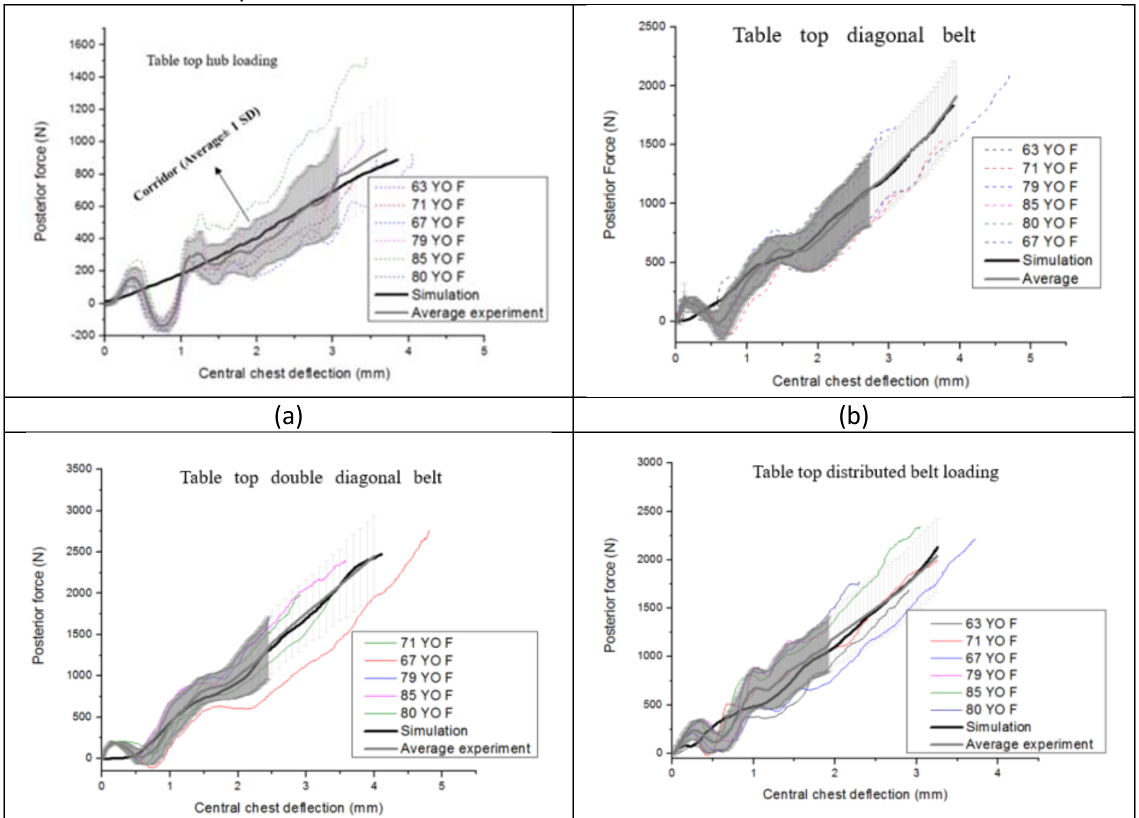

(a) (b)

(c) (d)

Fig. B8. Force-deflection curves from experiments and the simulation results for (a) hub loading, (b) diagonal belt, (c) double diagonal belt and (d) distributed belt.

Humerus 3-Point Bending

Duma *et al.* [34] conducted dynamic 3-point bending tests on humerus bones using a 9.48 kg impactor released from a drop height of 1.35 m. The impactor velocity was 3.64 m/s. In the simulation, an initial velocity of 3.64 m/s was assigned to a rigid impactor. The time histories of impact force and strain at interior location of the impact site were compared with the experimental data.

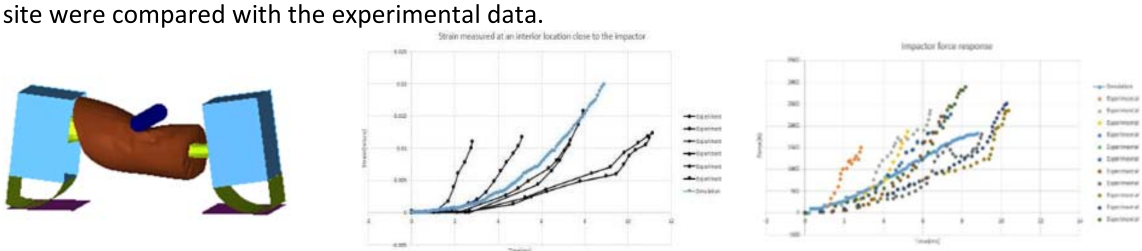

(a) (b) (c)

Fig. B9: (a) Simulation setup, (b) strain and (c) impact force time-histories.

Forearm 3-Point Bending

Duma *et al.* [34] conducted dynamic 3-point bending tests on forearm at supinated position. The impactor of 9.48 kg was dropped from a height of 2 m. The impactor velocity was 4.42 m/s. In the simulation, an initial velocity of 4.42 m/s was assigned to the rigid impactor. The peak moment at left and right support were measured and compared with the experimental data.

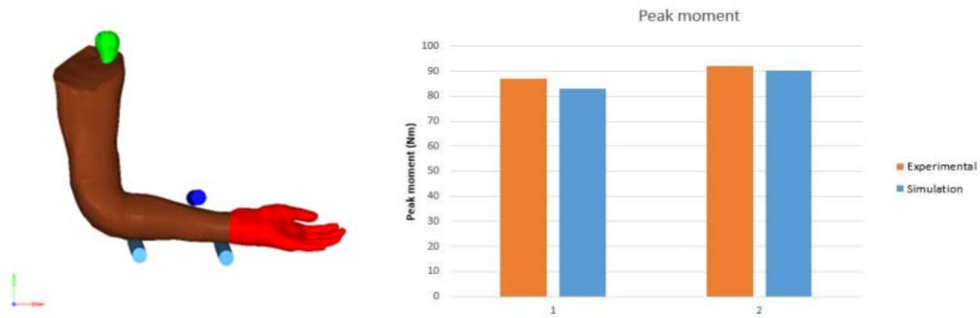

(a) (b)

Fig. B10: (a) Simulation setup and (b) peak moment of forearm impact simulation.

Lumbar Spine Bending

Demetropoulos *et al*. [30] conducted bending test on isolated lumbar segments. Flexion and extension at 4 m/s were applied to the cadaveric lumbar segments. During testing, the specimen was taken from an initially lordotic position through a high degree of flexion to end in kyphotic curvature. Bending moment vs. angle was reported. In the simulation, L5 was fixed and the lumbar segments were positioned so that axis of L1 was vertically down. The displacement time history was assigned to L1. Moment was exported from a cross-section plane between L5 and L4 for further comparison.

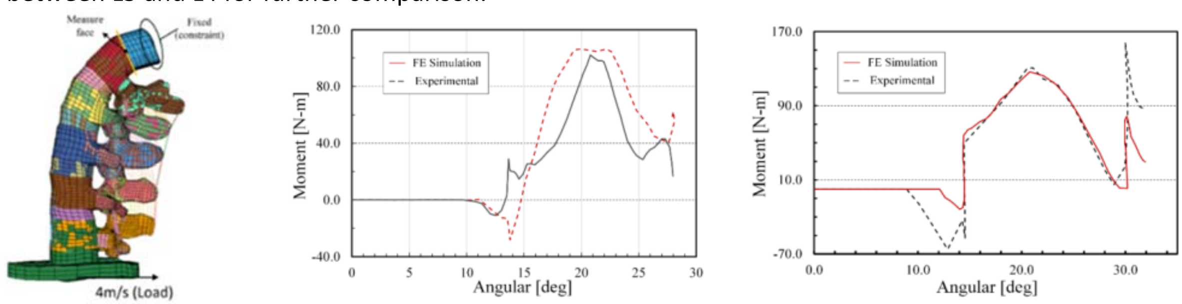

(a) (b) (c)

Fig. B11: (a) Simulation setup and model validation for (b) flexion and (c) extension.

Isolated Pelvic Ring Impact

The impact response of pelvis model was validated against the test results from Guillemot et al.[27]. Drop tests were conducted on 12 pelvic bones removed from cadavers with age ranged from 62 to 81, with a mean 70 years. A spherical metallic ball was fitted into the right acetabulum, to distribute the load all around the joint surface. The impactor was a 200 x 200 mm^2 metallic block with a total mass of 3.68 kg. The impacting surface was cushioned by silicon pad to avoid direct contact between rigid impactor and metallic ball. Impacting height was adjusted to obtain impact velocity of 4 m/s. From the simulation, the predicted maximum impact force and displacement was compared with the experimental data.

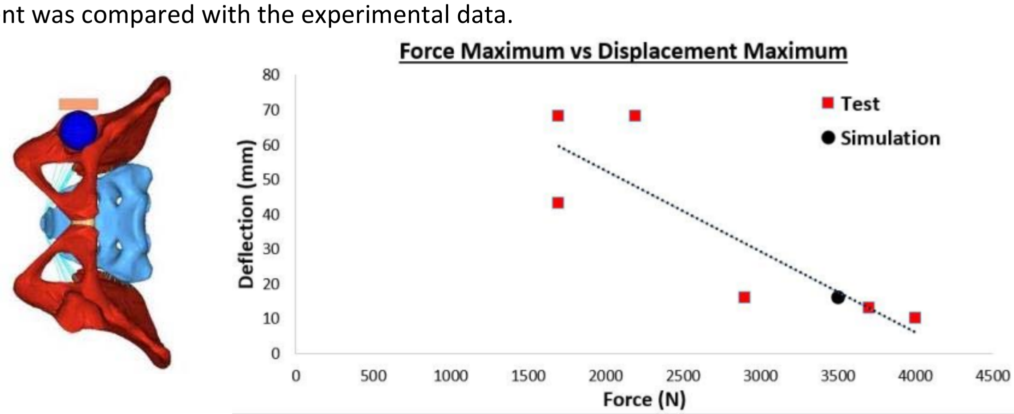

(a) (b)

Fig. B12: (a) Simulation setup and (b) model validation for maximum force vs maximum displacement.

Isolated Femur 3-Point Bending

To validate the behavior of femur in dynamic lateral bending, simulations were performed on the three-point bending test reported by Kerrigan et al.[31]. In this test, the femur was isolated from the body. Both ends of the femur were embedded in a pair of rotating potter. A rigid, cylindrical impactor with a radius of 6.35 mm and a length of 50 mm was used to apply dynamic impact loading at three locations (proximal one-third, midshaft, and distal one-third) with an impacting velocity of 1.2 m/s. Force-deflection curves at three bending locations were simulated and compared with the literature.

(a)

(b)

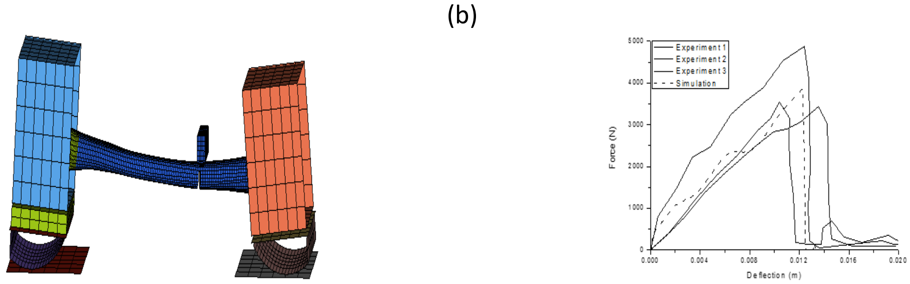

(c)

Fig. B13: Simulation setup (left) and model validation (right) at proximal (a), mid-shaft (b), and distal (c) regions.

Knee, Tibia, and Knee Bolster Impact

Viano et al.[32] performed bolster impact to knee and tibia on cadavers to assess the biomechanical response of lower-extremity impact and potential mechanisms of skeletal and ligamentous trauma. Padded knee bolster was used to perform three modes of impact: 1) tibia impact where knee joint for the leg flexed at 90°, 2) knee impact where knee joint for the leg flexed at 90°, and 3) knee-tibia impact where the knee joint for a leg flexed at 45°. Impactor mass was 55.9 kg. The impact surface was chosen to be square-faced 150 mm × 150 mm with a thickness of 57 mm pad for impact with 90° flexed and pad of 115 mm thickness with lower edge tapered for 45° flexed. Impacting speed ranges from 5.8 m/s to 6.4 m/s. From the simulation, peak impact force was compared with the literature.

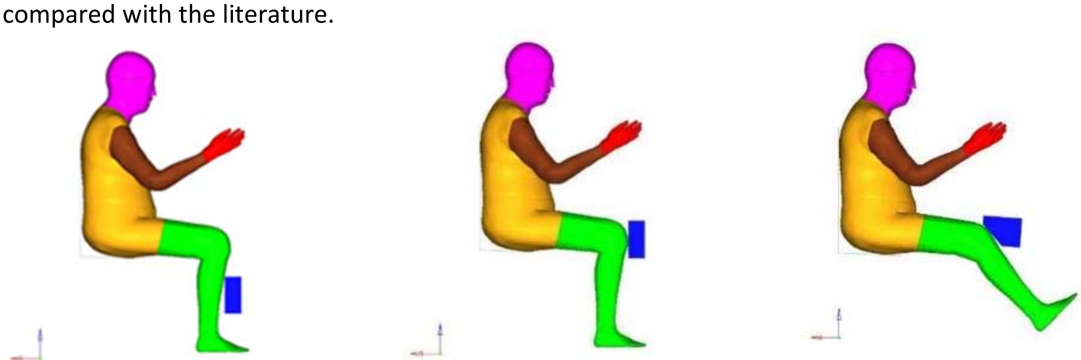

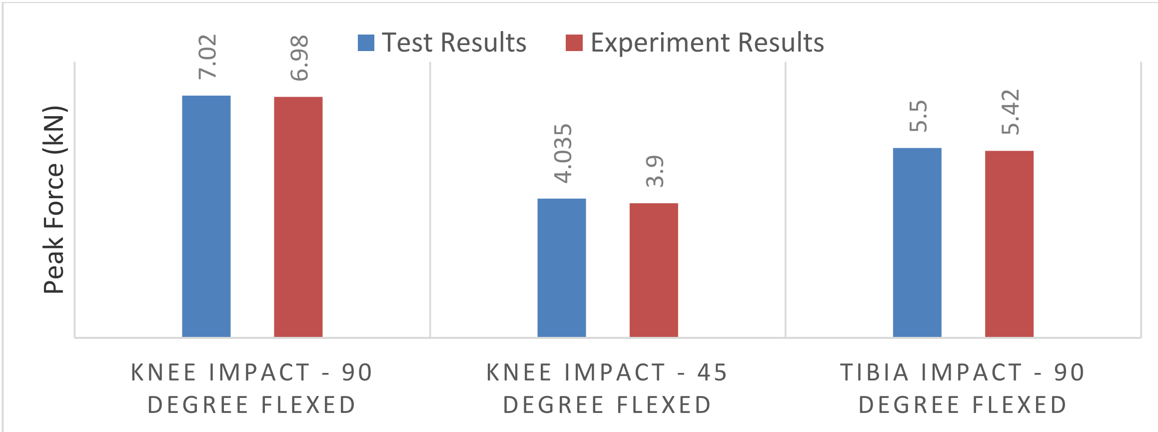

Fig. B14: Simulation setup (top) and peak force of test and simulation results (bottom).

Knee Bolster Impact on KTH (Knee-Thigh-Hip)

Rupp et al. [33] performed knee bolster impact on KTH. A linear impactor was used to impact KTH at 1 m/s along anterior-posterior direction and tibia was at 90° and 45° of knee flexion. Described motion was assigned to the rigid plate attached to the knee. Time history of impact force was compared with the reported data from the literature.

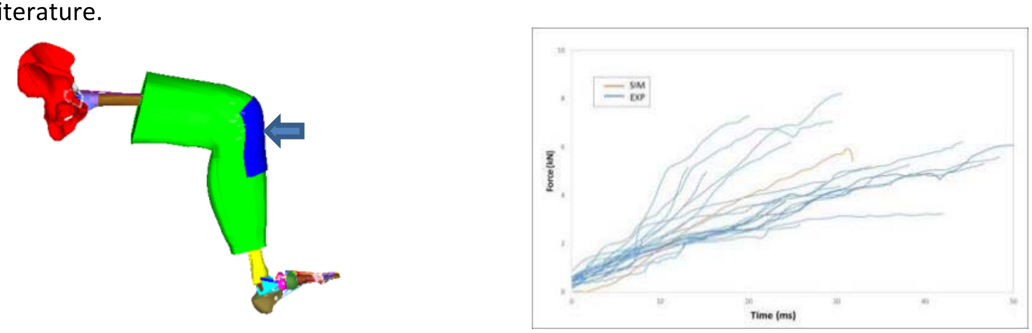

Fig. B15. Simulation setup (top) and peak force of test and simulation results (bottom).

Appendix C: Fringe plot of cortical strain distribution under belt loading

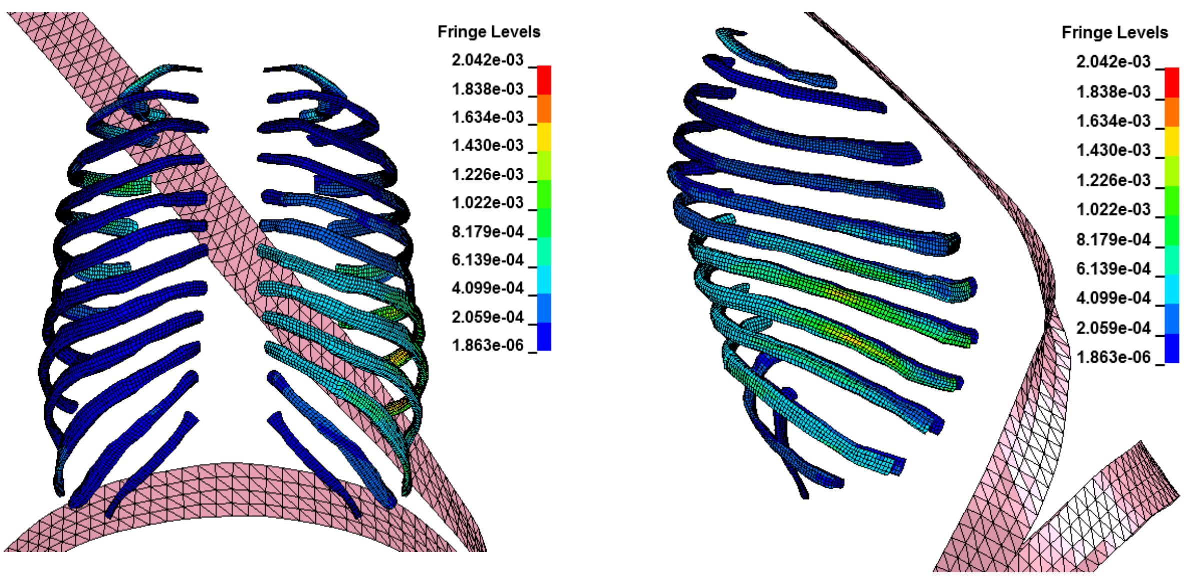

(a) Posterior View (b) Lateral View

Fig. C1. Fringe plot of effective strain distribution on rib cortical bone under belt loading

Appendix D: Mesh of CHARM-70F Model

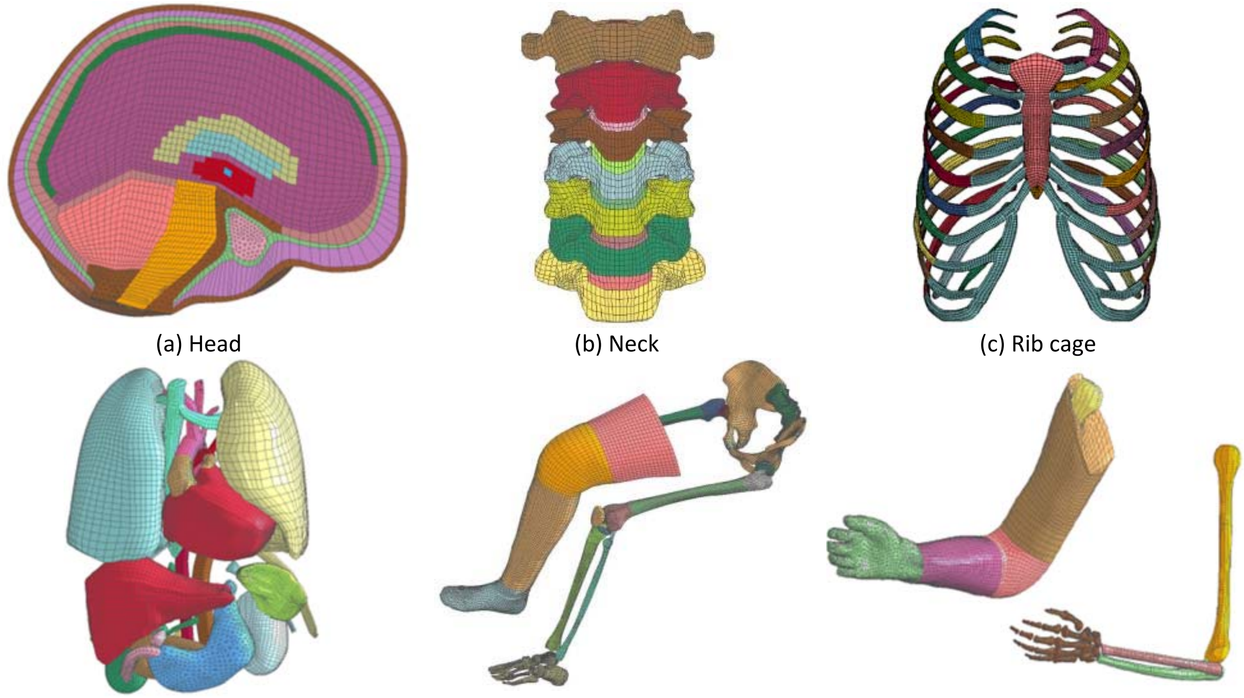

(a) Head (b) Neck (c) Rib cage

(d) Internal organs (e) Lower extremities (f) Upper extremities

Fig. D1. Mesh of CHARM-70F